River hydraulic modelling with ICESat-2 land and water surface elevation

Monica Coppo Frias[1,3], Suxia Liu[2,3], Xingguo Mo[2,3], Karina Nielsen[4], Heidi Ranndal[4], Liguang Jiang[6], Jun Ma[5] and Peter Bauer-Gottwein[1]

5 [1]Department of Environmental and Resource Engineering, Technical University of Denmark, 2800 Kgs. Lyngby, Denmark
[2]Key Laboratory of Water Cycle and Related Land Surface Processes, Institute of Geographic Sciences and Natural Resources Research/Chinese Academy of Sciences,100101 Chaoyang District, Beijing, China
[3]Sino-Danish College, University of Chinese Academy of Sciences, Beijing 100049, China
[4]Department of Geodesy and Earth Observation, Technical University of Denmark, 2800 Kgs. Lyngby, Denmark
10 [5]Hydrology Bureau, Yellow River Water Conservancy Commission, Zhengzhou, Henan, 450004, China
[6]School of Environmental Science and Engineering, Southern University of Science and Technology. 1088 Xueyuan Avenue, Shenzhen 518055, P.R. China

Correspondence to: Monica Coppo Frias (mcfr@env.dtu.dk)

Abstract. Advances in geodetic altimetry instruments are providing more accurate measurements, enabling satellite missions
15 to produce useful data in narrow rivers and streams. Altimetry missions produce spatially dense land and water surface elevation (WSE) measurements in remote areas where in-situ data is scarce, that can be combined with hydraulic/hydrodynamic models to simulate WSE and estimate discharge. In this study, we combine ICESat-2 land and water surface elevation measurements with a low-parameterized hydraulic calibration to simulate WSE and discharge without the need for surveyed cross section geometry and a rainfall-runoff model. ICESat-2 provides an opportunity to map
20 river cross-section geometry very accurately with an along-track resolution of 0.7 m using the ATL03 product. These measurements are combined with the inland water product ATL13 to calibrate a steady-state hydraulic model to retrieve unobserved hydraulic parameters, such as river depth or roughness coefficient. The low-parameterized model together with the assumption of steady-state hydraulics enables the application of a global search algorithm for a spatially uniform parameter calibration at a manageable computational cost. The model performance is similar to that reported for highly
25 parametrized models, with a root mean square error of around 0.41 m. With the calibrated model, we can calculate WSE time series at any chainage point at any time of an available satellite pass within the river reach, and estimate discharge from WSE. The discharge estimates are validated with in-situ measurements at two available gauging stations. In addition, we use the calibrated parameters in a full hydrodynamic model simulation resulting in a RMSE of 0.59 m for the entire observation period.

1 Introduction

Climate change affects the frequency and magnitude of extreme hydrologic events which are one of the major threats to human lives and ecosystems. Rainfall-runoff patterns are changing and with them the frequency of severe floods and

droughts, which are projected to increase with climate change (Masson-Delmotte V. and Zhou 2021), events that are reported to have a great impact on biodiversity (Chen, et al. 2022, Larsen, et al. 2019, Zhang, et al. 2021). Understanding how these altered patterns in rainfall-runoff affect WSE and inundation along rivers is fundamental for decision support and preservation of ecosystems, and reliable hydraulic models based on accurate observations are urgently needed. To create such models, WSE and bathymetry measurements are necessary. However, in-situ bathymetric surveys are scarce for remote river systems and such datasets are typically not in the public domain. Bathymetry estimates based on satellite remote sensing can thus create value for river monitoring and water resources management in inaccessible areas and ungauged river basins.

Hydraulic parameters such as riverbed geometry or hydraulic roughness are unobserved in many areas. Riverbed geometry is observable, but measurements require in-situ surveys, while river roughness is not directly observable at the required scales in natural rivers. On the other hand, WSE observations are more accessible and they play a major role in hydrologic research. Measurements of WSE are directly related to flooding patterns because flooding occurs when WSE exceeds critical thresholds. In addition, WSE is closely related to discharge in rivers and other hydraulic parameters (Jiang, et al. (2017)). During the last 20 years, satellite altimetry has been widely used to monitor WSE, including inland water bodies. Satellite altimetry has several advantages with respect to traditional survey methods. It provides wide spatio-temporal coverage reducing the time and cost of data collection. Missions such as Sentinel-3, CryoSat-2 or Jason-2 have been widely used in inland water monitoring and hydraulic calibration (Tarpanelli, et al. 2021, Chen, et al. 2022, Paris, et al. 2016, Villadsen, et al. 2015). However, these missions are limited to wide rivers due to their low spatial resolution (Shen, et al. 2020, Paris, et al. 2016) offering an along track resolution around 250-300 m. The future SWOT mission will be able to measure rivers down to 50 meters wide, and represents a promising opportunity for hydraulic models. Studies such as Garambois and Monnier (2015) or Pujol et al. (2020) show the potential of this mission, using synthetic SWOT observations. In terms of currently available datasets, the novel altimetry mission ICESat-2 which has been operating since 2018, offers an along-track resolution down to 0.7 m in the photon cloud product ATL03 (Neumann T., et al. 2021) and a variable resolution of a few meters in the ATL13 inland water product (Jasinski, Stoll, et al. 2021). The resolution of ICESat-2 provides an opportunity to measure WSE in narrow rivers.

Altimetry missions provide accurate elevation measurements at many cross-over points between satellite ground tracks and rivers, but at low temporal resolution. Cryosat-2, Sentinel-3 and ICESat-2 provide repeat passes every 369, 27 and 91 days respectively. Altimetry densification is a method that combines intermittent data from different cross-over points into a dense time series at specified points in space. This approach is used to enhance the low temporal resolution of altimetry missions. Studies such as Boergens, et al. (2016), Yoon et al. (2013) or Paiva, et al. (2015) use kriging interpolation approach, which makes predictions based on a linear combination of nearby observations. Another approach is interpolating WSE observations along the river, using WSE slope, as done by Villadsen, et al. (2015), which uses Cryosat-2 and Envisat data, or using ICESat-2 WSE measurements as in Scherer, et al. (2022). A recent study by Nielsen et al. (2022), proposes a statistical approach to build water surface time series from CryoSat-2, SARAL and Sentinel-3. However, the best estimators

of WSE in time and space are hydrodynamic models, which can be derived from altimetry data and respect the physical laws governing flow in open channels (Jiang, et al. (2017)). Moreover, calibrated hydrodynamic models are the best tool to define WSE- discharge relationships, where altimetry data can be used to update the states of the hydrodynamic model (Paiva, et al. 2013, Domeneghetti, Tarpanelli, et al. 2014).

Estimating bathymetry and roughness accurately in ungauged river basins is a very important task in the hydraulic modelling context and has been addressed in many studies (Durand, et al. 2014, Garambois and Monnier 2015). A common approach in the remote sensing framework is to derive bathymetry and roughness jointly using altimetric WSE observations. Studies such as Jiang, et al. (2019) use a spatially distributed bathymetry and roughness calibration using generic channel shapes where the roughness estimate presents ambiguity. The equifinality issue has been also discussed in Pujol, et al. (2020) who introduced prior parameter information and river widths from optical imagery on top of SWOT WSE synthetic observations to infer distributed channel parameters. Bjerklie et al. (2018) includes observations of water surface area from Landsat observations and water surface slope from Jason-2 and ICESat. Even with the introduction of new satellite signatures into the hydraulic model, equifinality remains a challenge. The ICESat-2 ATL03 product offers an opportunity not only to measure river widths but also to map the exposed portions of the river bed at a high spatial resolution, improving the quality of riverbed geometry data sets for hydraulic simulations. With this approach we can reduce the non-uniqueness in the parametrization because it is not necessary to estimate the full bathymetric profile.

Hydrodynamic model calibration of river parameters requires significant computational resources, since solving the Saint-Venant equations requires short time steps (typically on the order of minutes) resulting in long simulation times for seasonal or multi-year periods. Thus, inverse modelling workflows, where the forward response has to be evaluated at least thousands of times, need model simplifications, especially when global search algorithms are used. Studies such as Jiang et al. (2019) estimate distributed bathymetry and roughness along the river channel in a regularized inversion framework using local gradient search methods. A constrained parameter space will greatly help in reducing computation time, therefore, the number of distributed parameters should be limited. Kittel et al. (2021) proposed to use a steady state version of the Saint-Venant equations that significantly reduces computational time in the calibration process, providing a reasonable representation of river channels to be used in a full hydrodynamic simulation.

The aim of this paper is to combine ICESat-2 land and WSE datasets with river hydraulic modelling. We use the modelling approach by Kittel et al. (2021) with a spatially uniform parametrization, including elevation measurements at a cross-section level from the ATL03 photon cloud product. This is an important step towards retrieval of hydraulic parameters that are often unobserved or unobservable at relevant spatial scales such as Manning's roughness or river depth, and to reduce the equifinality issues related to highly parametrized models. Hydraulic characterization of river channels enables the conversion of discharge to WSE and vice-versa. This study proposes a method to estimate discharge from ICESat-2 WSE observations. In addition, the WSE observations and discharge estimations are densified in space and time. With this approach, we produce dense time series and overcome the spatial and temporal sampling limits that characterize altimetry missions, which are critical in narrower river channels (<250 m).

2 Study Area

The Yellow River is the second longest river in China and the sixth longest in the world. The total length of the river is around 5464 *km* and it has a drainage area of about 795.000 km^2. It rises in the Qinghai province of western China, in the Bayan Har Mountains. The high-flow season occurs during the rainy season, between June and October, and the low-flow season is between November and May.

Our focus is the Upstream Yellow River (see Figure 1), starting at its source in the Bayan Mountains and flowing to Tangnaihai, where elevations are above 3600 m above mean sea level. The total basin area is about 386.000 km^2. We select a river stretch between Jimai and Mentang, with a distance along the channel about 300 km. Jimai is located at 33°46′12″N, 99°39′25″E at an elevation about 3950 meters above mean sea level, and Mentang is located at 33°46′12″N, 101°2′60″E at an elevation about 3630 m above mean sea level. The river section just downstream of Jimai is characterized by alluvial plains for about 50 km and becomes narrower with steep cliffs lining both sides of the river until it reaches Mentang. This river stretch is characterized by a narrow river width, corresponding to 80-180 meter in low-flow season with curved bedforms, and dominant west-east orientation, making it a good example to demonstrate the ability of ICESat-2 data in narrow river channels.
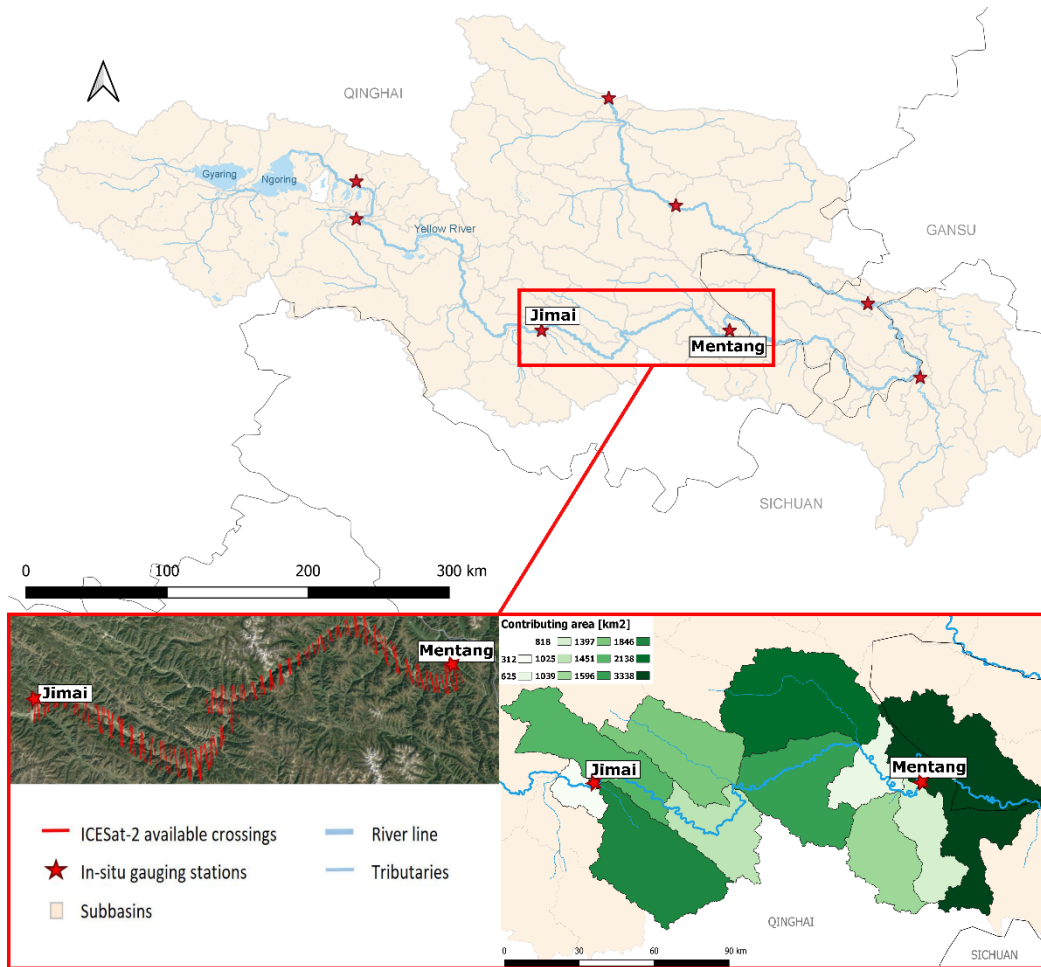
Figure 1. Area of interest and in-situ gauging stations in the Upstream Yellow River. Calibration is performed for the river reach between Jimai and Mentang (zoom). The bottom right image represent the catchment area along the river reach. The bottom left image shows the ICESat-2 crossings available in the river stretch.

3 Data

3.1 ICESat-2

ICESat-2 is an altimetry mission operating since November 2018. This mission has 1387 reference ground tracks (RGTs) that are measured every 91 days. Each RGTs contains 3 pairs of ground tracks, each pair formed by a strong beam and a weak beam. The strong and weak beams have transmitted energy of 175 µJ per pulse and 45 µJ per pulse respectively (Neumann T., et al. 2021). The strong-weak beam pair is separated by 90 m and each pair of beams is separated by 3.3 km. With this configuration, ICESat-2 provides a wide inter track spatial coverage, covering large areas with altimetric measurements.

5

ICESat-2 data is acquired from the National Snow Ice Data Center (NSIDC) portal and the National Space Institute, Technical University of Denmark (DTU Space) database for the period between 31/10/2018 to 02/04/2021. Two different product levels are used: ATL03, ATLAS/ICESat-2 L2A Global Geolocated photon Data and ATL13, ATLAS/ICESat-2 L3A Along Track Inland Surface Water Data, both having a temporal resolution of 91 days.

The pulse repetition frequency of ATLAS corresponds to an along track resolution of 70 cm. Depending on the number of photons that return to ATLAS, the ATL03 product can offer an along-track resolution down to 0.7 m and provides the geolocated photon event down-linked from ATLAS. The signal photon events are distinguished from the background events by calculating the signal-to-noise ratio. We use this product to map the land topography of the river cross-section and measure hydraulic parameters such as river flow width and WSE as explained in section 4.1.1.

ATL13 product provides inland WSE with an ensemble error of 6.1 cm per 100 inland water photons (Jasinski, Stoll, et al. 2021) . The along-track resolution of this product varies, but is typically of the order of a few meters. We use this product to extract mean WSE at river crossings, for the steady state model calibration. The ATL13 data is prepared for the period between 31/10/2018 to 21/09/2020. In addition, there is a validation dataset in the period from 13/12/2020 to 19/10/2021. The periods for the calibration and validation datasets are defined according to the in-situ discharge observations available at Jimai and Mentang gauging stations (see section 3.2).

3.2 In-situ data

In situ observations from Jimai and Mentang gauging stations were kindly provided by the Yellow River Conservation Commission (YRCC). The available data covers the period between 10/05/2018 and 21/09/2020. Discharge data at both stations are used as boundary conditions for the steady-state hydraulic model, that simulates WSE along the river reach from given discharge. Jimai station provides data for both low-flow and high-flow season, while Mentang station is missing the data for the low-flow season. Data from the period between 13/12/2020 to 19/10/2021 is available to validate the model.

3.3 Ancillary datasets

A 3-arcsec Digital Elevation Model (DEM), flow accumulation map and flow direction map are downloaded from MERIT global database (Yamazaki, et al. 2019). A conceptual river basin model is developed, in which the major runoff generating catchments are identified at the main tributaries of the river reach. TauDEM is used to delineate the river network and catchments with the information extracted from MERIT database (Yamazaki, et al. 2019). The river delineation is used as reference for the river centre-line when defining river cross-sections. The chainage of the river is generated from the river delineation with steps of 10 m, referenced to Lake Eling, close to the river source in the Bayan Har Mountains. The water occurrence map is downloaded from the Global Surface Water Explorer (Pekel, et al. 2016). The water occurrence is used to filter the WSE observations from ATL13.

4 Methods

An overview of the workflow, including different data processing and modelling steps, is presented in Figure 2. The method uses two different ICESat-2 data products as inputs and a steady-state 1D hydraulic model in the inverse hydraulic parameter
160   calibration process. The ATL03 and ATL13 products are processed (see sections 4.1.1 and 4.1.3) to be ingested together with in-situ discharge data in a hydraulic model calibration to estimate river flow depth, roughness coefficient and river bed shape. The calibrated model is used to calculate rating curves relating discharge and WSE and interpolate WSE time series along the river stretch. In addition, the parameter values are used to run a full 1D hydrodynamic simulation.
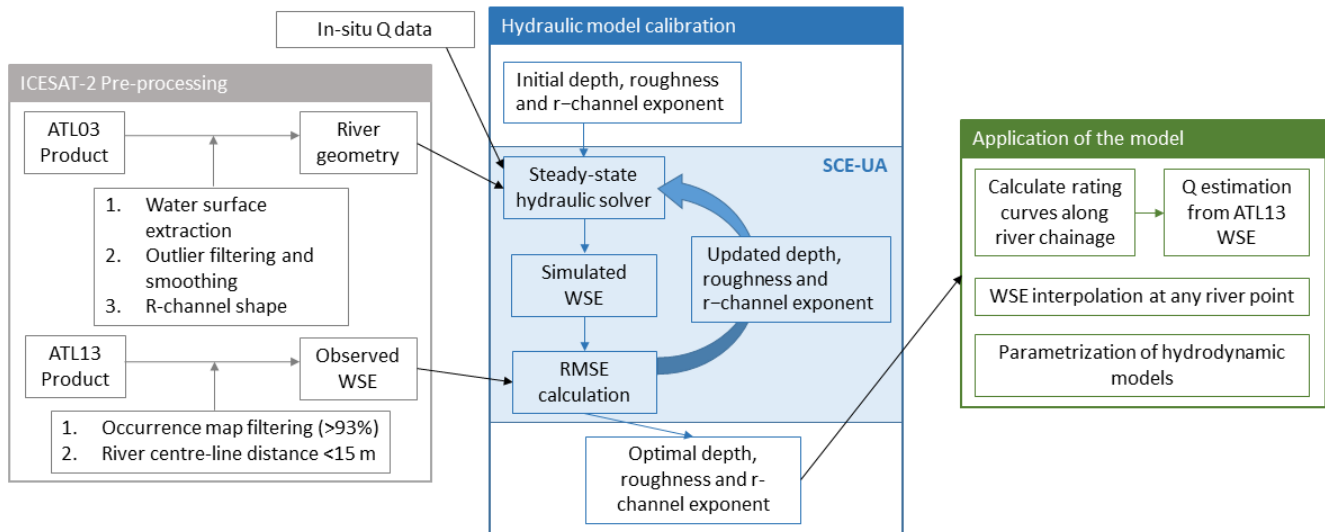
165   **Figure 2.** Schematic diagram of the data processing and modelling workflow in this study. The methodology proposes a series of applications from a calibrated model.

4.1 ICESat-2 land and WSE data processing

4.1.1 ATL03 cross-section processing

The ATL03 photon cloud product is used to define riverbed geometry. To ensure that as large a portion of the river bed as
170   possible can be extracted from ICESat-2 observations, only the low-flow season crossings are taken into account, corresponding to the period between November and April. In addition, to select good-quality cross-sections, visual inspection is also performed. The strong beam and weak beam data, separated by 90 m, were observed to behave differently depending on the acquisition date. For the cases in which the strong beam signal was very strong, the data can present noise that complicates the processing steps, the weak beam crossing is selected. For acquisitions with weaker signals, the
175   topography is better mapped by the strong beam signal.

The water surface in the ATL03 data is characterized by a dense cloud of photons. A Gaussian Kernel distribution is used to identify the water surface by taking the peak density value of the distribution. The points between 20 cm from the peak value

are also identified as water surface and averaged. The river width is computed as the along-track extent of the water surface, taking into account the crossing angle between ICESat-2 ground-track and river centre line.

180 To remove outliers from the photon cloud, two different methods are used: firstly, a Hampel filter is applied, in which the Median Absolute Deviation (MAD) is computed for a sliding window in a 3.5 m ground-track interval. A value will be considered an outlier if it exceeds the MAD. The MAD is defined as in equation (1):

$$MAD = median(|X_i - \widetilde{X}|) , \tag{1}$$

with $\tilde{X} = median(X)$ After the Hampel filter, a Median filter is applied for the same 3.5 meters ground-track intervals. The

185 ground-track interval is a "window" that slides entry by entry, and replaces each entry value by the median of the neighbouring entries. Finally, in order to obtain a well-defined shape of the river cross-section, a Simple Moving Average (SMA) is computed for ground-track intervals of 3.5 m.

4.1.2 R-shape geometry for submerged portion

In the submerged portion of the channel, the ATL03 product does not detect the riverbed elevation. ATL03 product can

190 successfully map bathymetry for clear waters, as shown by Parrish et al. (2019), who present results mapping seafloor bathymery. The portion of the Upstream Yellow River we focus on (see section 2), is characterized by fast and turbulent flow, which explains why bathymetry cannot be detected by ICESat-2 in this area. To cope with this limitation, the riverbed elevation in the submerged portion of the river is extrapolated using the approach proposed by Dingman (2007), that has been previously used for discharge estimates in Bjerklie et al. (2018). The shape of the submerged portion depends on a

195 cross-section form exponent r, with r = 1 corresponding to a triangle and r → ∞ corresponding to rectangular shape. The height above the lowest channel elevation, z, is approximated by equation (2),

$$z = Y_m^* \left(\frac{2}{W^*}\right)^r x^r, \qquad 0 \le x \le W^*/2, \ , \tag{2}$$

where Y_m^* is the low-flow depth, W^* is the bank width, and x is the horizontal distance from the river centre-line. Figure 3 shows the different processing steps applied to ATL03 data to define the river bed geometry. In the last step, the submerged

200 portion is interpolated, thus for each cross section, there are two free parameters Y_m^* and r that will be estimated in the hydraulic inversion (see section 4.3).
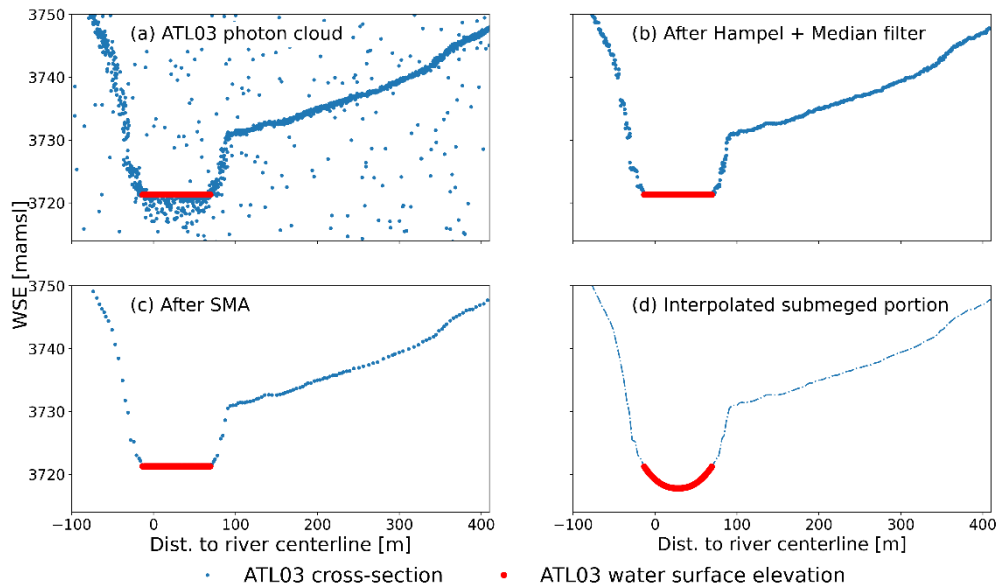
Figure 3. ATL03 photon cloud, where the water surface is identified (a). The outliers are removed using Hampel and Median filter (b). Smoothing of the cross-section with SMA (c), and interpolation of the submerged portion (d).

4.1.3 ATL13 data processing

The model calibration needs an adequate selection of WSE data from ATL13 or other suitable altimetry missions. Radar altimetry missions, such as Cryosat-2 or Sentinel-3 cannot provide high-accuracy measurements in this area due to their low spatial resolution (250-300 m). The river stretch we focus on, has river width varying between 80 meters in the low-flow season, to few hundred meters in the high-flow season. The ATL13 product offers a variable resolution depending on the acquisition date, but it is normally of the order of few meters (Jasinski, Stoll, et al. 2021). This ICESat-2 product offers a variety of data quality flags to discard invalid measurements. In Xu et al. (2021) the following flags are considered for WSE assessments: *qf_bckgrd, qf_bias_em, qf_bias_fit*, *stdev_water_surf* and *snow_ice*. These flags control the density of background photons, electromagnetic bias, and bias in the fit, standard deviation of WSE and presence of snow or ice. After applying the flags, Xu et al. (2021) recommend an extended outlier filtering method. Moreover, the ATL13 data product presents known issues, such as including land area adjacent to WSE or land measurements in the low-flow season that need to be considered (Jasinski, Stoll, et al. 2021).

The morphological characteristics of the river make the selection of good WSE observations challenging. The river stretch presents braided structures in selected areas, in which ATL13 product can mix the land in between channels with water surface. To avoid this issue, we first apply the water occurrence map from Global Surface Water Explorer (Pekel, et al. 2016), only including observations that fall over pixels with water occurrence larger than 93%, a threshold that is exceeded in very few pixels. Taking into account the river delineation extracted from the MERIT database (Yamazaki, et al. 2019) (see section 3.3), we only consider WSE points that are less than 15 m away from the river centre-line, to ensure that ATL13

9

observations fall in the water surface in the low-flow period, when we have flow widths around 80 m for selected areas. The points that are within 15 m from the river centre-line are averaged to have a unique observation for different dates at every chainage point. In addition, all the WSE measurements within the same acquisition date, that are less than 500 m away from each other, and where the WSE variation is less than 15 times the slope times the distance between observations are averaged. This last criterion is taking into account the computational grid resolution of the hydraulic model, which is 300 m and refined to 100 m in selected areas (see section 4.2).

We compared the performance of the filtering process with the quality flags, taking the values proposed by Xu et al. (2021) , $qf\_bckgrd < 6$, $|qf\_bias\_em| < 2$, $|qf\_bias\_fit| < 2$, and constraining the water surface standard deviation, $stdev\_water\_surf$ to 0.5 m. The $snow\_ice$ flag was also applied, with no presence of ice for the area of interest. The results are better when we filter with respect to the river centre-line and water occurrence map, than using the ATL13 quality flags. After applying the quality flags only, some of the points that fall on adjacent land area are not removed.

4.1.4 Cross-sections and observation points selection

Cross-sectional data from ATL03 is selected for the available dates in the low-flow season. Depending on the acquisition dates, the discharge varies and, accordingly, the reference WSE of the cross-section changes. This can lead to unreasonable variations in the bottom elevation when constant depth is assumed leading to simulation errors. To avoid such errors and have a realistic reference bottom level (BL), we define a reference WSE. The reference WSE is taken from the ATL03 cross-section in which the acquisition date has the lowest discharge value from the in-situ data. The discharge variation is calculated between the lowest in-situ discharge value and the in-situ discharge values for ATL03 cross-section acquisition dates. Since the discharge variation should be proportional to the WSE variation, we define a correction factor α relating discharge variation to WSE variation as $\Delta WSE = \alpha \cdot \Delta Q$. The correction factor α is a calibration parameter, and we add $\alpha \cdot \Delta Q$ to the corresponding cross-section depth value.

To confirm that the discharge variation and the WSE between ATL03 and ATL13 are consistent, we compare the WSE measured by the ATL03 and the ATL13 for the values that are closer 300 m, according to the resolution of our model, and the variation of discharge between the ATL03 and ATL13 acquisition dates. The analysis can be seen in Figure 4 (a). The method we use to detect the WSE in the ATL03 product is different from the one used to produce the ATL13 product (see section 4.1.1), hence we can find differences between our detected WSE and the one provided by ATL13 product for the same acquisition data. An example of the difference between WSE detected in ATL03 and ATL13 WSE can be seen in figure 4 (e), where there is an offset between elevations of about 0.41 m. This would explain some of the points that lie close to $\Delta Q = 0$ for which ΔWSE is different from 0 in figure 4 (a). To avoid this problem, we substitute the WSE at each ATL03 cross-section, by the value given in the ATL13 product, and the submerged portion is interpolated based to this value. By substituting these values, some of the discharge variations that were not in accordance with the WSE variation were corrected, for example, the value lying close to $\Delta WSE = 0$ and $\Delta Q = 400$ in Figure 4 (a) lies closer to $\Delta WSE = 1$ in Figure 4 (b).

In addition, the Jimai rating curve presents some anomalies (Figure 4 (c)), in which the pair discharge-WSE does not follow the power law (points with low discharge values have a high WSE value), that could be explained by the freezing of the water surface in the station area. We observed that the outliers in Figure 4 (a) were related to the rating curve anomalies (Δ

260 WSE around 2 m and ΔQ close to -200m^3/s), and the ATL03 and ATL13 data taken at the corresponding dates were rejected. After this analysis, the resulting relation between ΔQ and ΔWSE can be seen in Figure 4 (a).
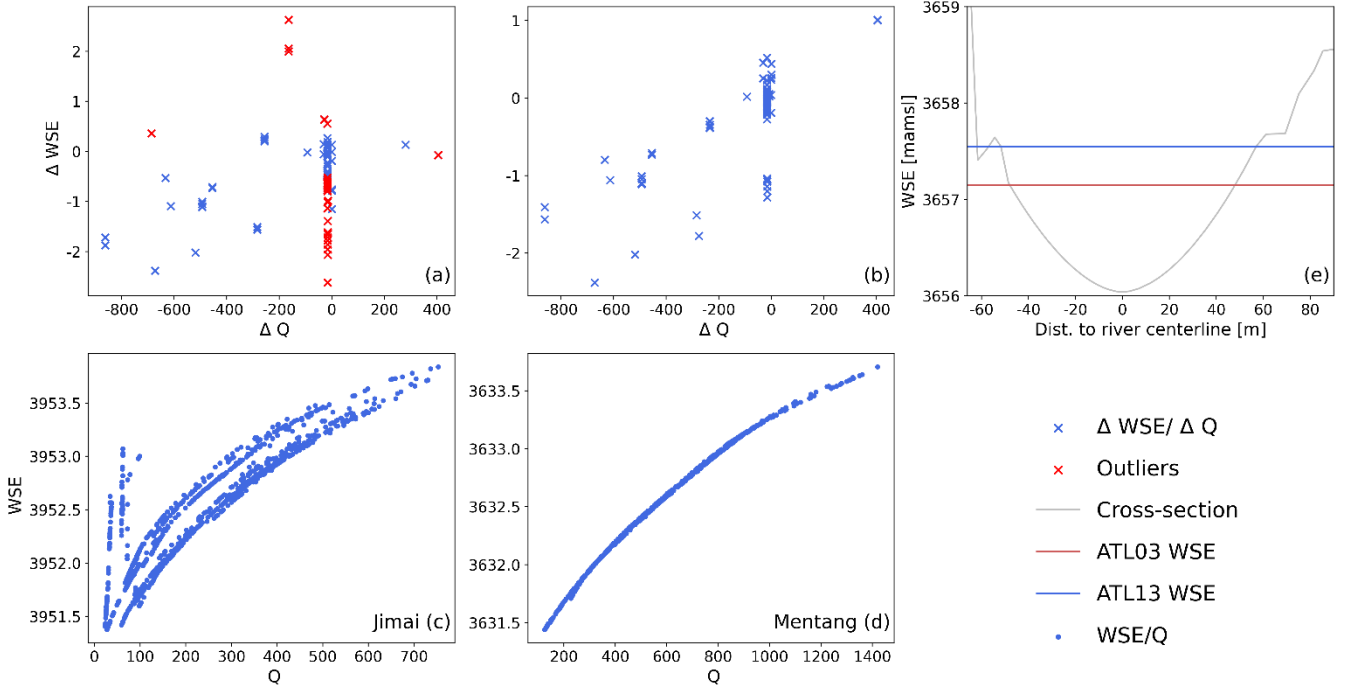
Figure 4. Variation of discharge against WSE from ATL03 and ATL13 (a). Variation of discharge against variation of WSE from ATL03
265 and ATL13 after correction (b). Rating curve (discharge against WSE) for Jimai gauging station (c). Rating curve for Mentang gauging station (d). Example of mismatch between ATL13 and ATL03 WSE (e).

4.2 1D Hydraulic model

The 1D hydraulic model is defined assuming steady state. This assumption is reasonable for ATL13 observations after filtering and checking that discharge varies consistently with WSE (see sections 4.1.3 and 4.1.4). The steady-state hydraulic

270 solver is based on the Saint-Venant equations in steady state. These equations express the mass and momentum balance in an open channel as given by equation (3).

$$q = \frac{\partial A}{\partial Q} + \frac{\partial Q}{\partial x}, \qquad \frac{\partial Q}{\partial t} + \frac{\partial}{\partial x}\left(\frac{\beta Q^2}{A}\right) + gA\frac{\partial h}{\partial x} - gA(S_0 - S_f) = 0 \; , \qquad (3)$$

The steady-state assumption implies constant discharge over time, hence all time derivatives are zero. The x is the chainage or distance along the channel, h is channel depth, A is the flow cross-sectional area, q is the lateral inflow, Q is the discharge,

11

275 S_0 and S_f are the bed and friction slopes respectively, g is the gravitational constant and β is the momentum coefficient which is set to 1.

From the steady state solver, we calculate WSE profiles from a given discharge and water level at the downstream point as described in Kittel et al. (2020). The WSE is computed step-wise at Δx spatial increments and moving upstream along the channel. The equation to solve is presented in (4), which is based on the steady state Saint-Venant equations assuming

280 subcritical fluvial flows and where right hand side (RHS) is the collection of terms not containing the derivative of the depth with respect to the chainage (see Kittel et al. (2020) for the full derivation).

$$RHS(x, h(x)) = \frac{\left(\frac{Q^2}{gA^3} \frac{\partial A}{\partial x} + S_0 - \frac{Q^2}{K^2} - \frac{2Q\,q}{gA^2} \right)}{1 - \frac{Q^2}{gA^3} \frac{\partial A}{\partial x}} \; , \tag{4}$$

The model is initialized by calculating the downstream WSE from in-situ discharge assuming uniform flow and using Manning's equation and the local slope bed value between the two most downstream cross-sections. This value is initialized

285 at 0.0011 *m/km* and updated at each iteration. Equation (4) is solved explicitly as expressed in (5):

$$h_{i-1} = h_i - RHS(x_i, h_i) \cdot \Delta x \; , \tag{5}$$

The chainage grid is defined with step increments of 300 m in between observed cross-sections when the slope is less than 0.20 *m/km*, for the sections of the river reach with steeper slope (≥ 0.20 *m/km*) or areas in which neighbouring cross-sections present a significant difference in low-flow width, the step increment is reduced to 100 m to avoid instability of the explicit

290 numerical scheme. To make sure that model results are independent of the chosen grid discretization, different forward runs were made for step size down to 50 m, and differences in simulated WSE was shown to be insignificant.

4.2.1 Boundary conditions

The downstream boundary is defined as a free uniform outflow boundary condition (Li, et al. 2017). This boundary is defined 10 km away from the downstream station, by duplicating the ATL03 cross-section defined closest to Mentang

295 station. To initialize the steady state solver, a value of WSE at the downstream point is calculated from in-situ discharge values, using Manning's equation.

The lateral inflow q is distributed along the chainage proportionally to the contributing area (see Figure 1), taking into account the discharge variations from upstream and downstream in-situ data. The lateral inflow at chainage x is computed as in equation (6).

300 $q = \frac{Q_x - Q_{x-1}}{\Delta x} \; , \tag{6}$

To calculate the discharge at chainage x, Q_x, we assume that the runoff in the catchment is uniformly distributed, i.e. boundary inflow is proportional to the increment in contributing area, defined by the term upstream drainage area (UPA), which is available in the MERIT dataset (see section 3.3). Instead of calculating a rainfall run-off model, we use in-situ

discharge measurements at two available stations Jimai (upstream discharge Q_{up}) and Mentang (downstream discharge Q_{down}) (see section 2). For the downstream station, Mentang, the available data is between May and November, while for the upstream station, Jimai, there is data available for the whole period. Hence, two possible scenarios are taken into account:

1. If in-situ observations are available at both upstream and downstream stations, the distributed discharge at chainage point x is as in 7,

$$Q_x = Q_{up} + \frac{UPA_x - UPA_{up}}{UPA_{ds} - UPA_{up}}(Q_{ds} - Q_{up}) \ , \qquad (7)$$

2. If only upstream in-situ data is available, which is the case for the low season period (October to May), we consider the discharge at chainage point x is as in equation 8.

$$Q_x = Q_{up} + \frac{UPA_x - UPA_{up}}{UPA_{up}}(Q_{up}) \ , \qquad (8)$$

4.3 Parameter estimation

The objective of the parameter estimation is the retrieval of river bed geometry characteristics, i.e. Y_m^* and r (eq. 2) as well as Manning's roughness for each cross-section. To estimate the hydraulic parameters, model calibration is performed for four spatially uniform parameters: low-flow depth, Manning's roughness, r-shape exponent and a correction factor alpha. The calibration algorithm we use is the Shuffled Complex Evolution from the University of Arizona (SCE-UA) presented by Duan et al. (1992) and implemented in Python using Spotpy (Houska, et al. 2015). The SCE-UA is a global optimization algorithm that samples the parameter space using complexes. Each complex is evolved independently according to the competitive complex evolution (CCE) presented by Nelder and Mead (1965) and shuffled (re-partitioned) after each evolution to ensure an efficient global search. For the method to give a better overall performance, the number of complexes is set to $2n + 1$ where n is the number of parameters (Duan and Sorooshian 1993), in our optimization algorithm we work with 9 complexes. The objective function is the standard deviation of the prediction error between the ATL13 WSE and the simulated WSE, known as the Root Mean Square Error (RMSE):

$$Obj = \sqrt{\frac{1}{N}\sum_{i=1}^{N}(WSE_{sim} - WSE_{ATL13})^2} \ , \qquad (9)$$

The low-flow depth varies between 1.3 and 2.5 m and its initial value is 2 m, the Manning roughness varies between 0.027 and 0.06 $s/m^{1/3}$ and it is initialized at 0.031 $s/m^{1/3}$, the r-shape exponent varies between 1 and 3 and it is initialized at 1.8 and the correction factor alpha varies between 0.0005 $m/m^3/s$ and 0.003 $m/m^3/s$ and it is initialized at 0.002 $m/m^3/s$. For the parameter prior distribution, we choose a uniform distribution. The sensitivity of the parameters in the model calibration is computed using Fourier amplitude sensitive test (FAST) proposed by Saltelli et al (1999).

4.4 Lateral inflow analysis

To produce good estimates of WSE and discharge from a 1D hydraulic model, the inference of adequate parameters and definition of boundary conditions is fundamental. The main source of uncertainty in the model comes from the lateral inflow, for which measurements are not available. The lateral inflow boundary is defined using the MERIT flow accumulation map, as explained in section 4.2.1. To study the sensitivity of the model to the lateral inflow definition, we also run a calibration assuming uniform lateral inflow along the simulated chainage interval. Since the MERIT flow accumulation accounts for the tributary contributions, we expect that the model performance will degrade when uniform lateral inflow is assumed instead of uniform runoff.

4.5 Application and use cases

4.5.1 WSE densification and discharge retrieval

The calibrated model reproduces WSE-discharge relationships in the form of rating curves. We produce a series of rating curves along the river stretch for a given downstream discharge value to create a look-up table between river chainage, WSE and discharge. This relation can be used for different applications:

1. Densification of WSE: This is the aim of several studies, which use different methods to interpolate altimetry WSEs, using Kriging methods (Boergens, et al. 2016, Yoon, et al. 2013) or interpolation using WSE (Villadsen, et al. 2015). In our case, we use the calibrated 1D hydraulic model to calculate WSE along the river stretch. Using ATL13 observations at different acquisition times, we can predict WSE at any river point using the calibrated model.

2. Discharge retrieval: The calibrated model can be used to convert ATL13 WSE observations into estimates of river discharge using WSE-discharge relations (Malou, et al. 2021) . At any time of ICESat-2 acquisitions or any other type of altimetry data, we can ingest an observation of WSE to produce discharge estimates in any point of the river stretch using the estimated rating curves from the 1D hydraulic model.

4.5.2 Parametrization of HD models

The optimal parameters from the 1D hydraulic calibration can subsequently be transferred to a full hydrodynamic model simulation if predictions of dynamics of discharge and WSE are of interest. To demonstrate the ability of the method in the parametrization of full hydrodynamic simulations in the transient state, we use MIKE Hydro River (Havnø, Madsen and Dørge 1995). This is a 1D hydrodynamic model that uses a dynamic wave solver of the 1D Saint-Venant equations. To run the hydrodynamic model we use daily in-situ discharge data as an upstream boundary for a period of 3 years. MIKE Hydro River uses the calibrated cross-sections to get information on calibrated channel geometry and optimal Manning's roughness coefficient. The runoff increments are distributed according to the contributing area, which is obtained from the MERIT flow accumulation map.

5 Results

5.1 ICESat-2 data processing

365   ### 5.1.1 ATL03 cross-sections processing and selection

The cross sections are visually inspected to identify if the land and water topography are well defined, and there are no signs of cloud formation or weather effects. 80 ATL03 cross-sections are selected, which define the river bed geometry along the river reach between Jimai and Mentang (see Figure 5 bottom), including measurements of land elevation of the dry portion of the riverbed. Measurements are provided every 3.5 to 20m. Closely spaced cross-sections are removed to reduce the

370   computational cost of the model since only cross-sections whose chainage differs more than 500 m provide meaningful information due to the resolution of the 1D hydraulic model. In areas with scarce ICESat-2 data, there can be a separation between cross-sections up to 10 km. The gaps in the data at the scale of our investigation are mostly due to the poor quality of acquisitions, in the period in which weather conditions are having an impact on the ICESat-2 observations. For the river stretches with little cross-section information, we interpolate cross-section in between using the MIKE Hydro River cross-

375   section module, however model performance is expected to be worse here.
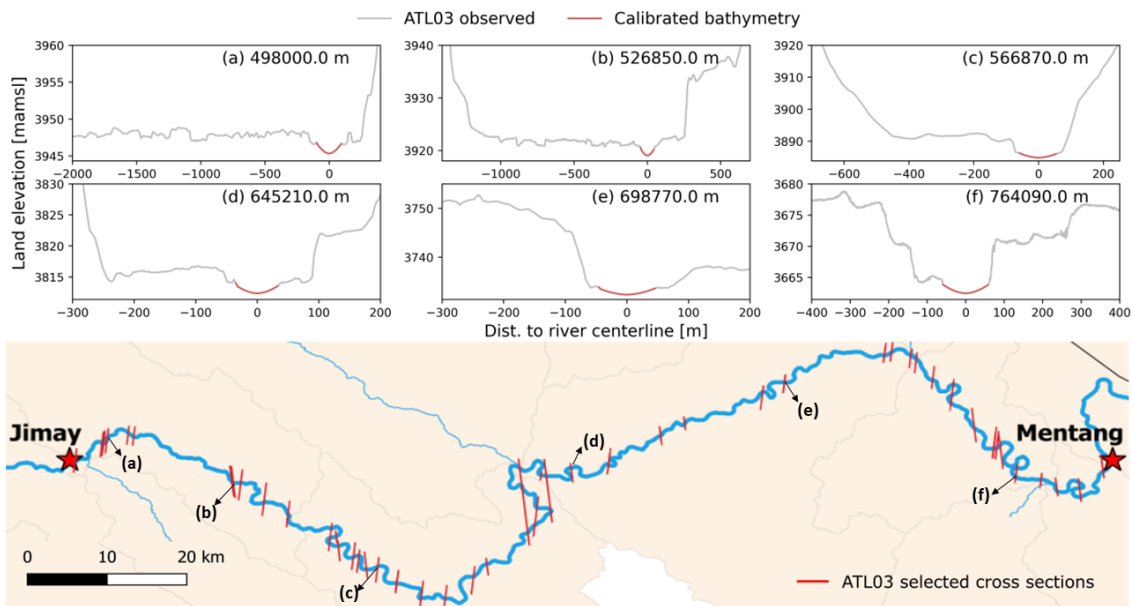
Figure 5. Top: Examples of cross section geometry after calibration, where the majority of points correspond to ATL03 observed data. Bottom: ATL03 selected cross-sections for river hydraulic calibration. 80 cross-section were selected after processing described in section 2.1.1. The cross-section shown in the top plot are located in the river.

380   The top panel of Figure 5 gives examples of the cross-section geometry measured with ATL03 together with submerged portion that is not observable and has been calibrated. These cross-sections give quite a reasonable representation of the river geometry. An advantage of the method is that most of the cross-section points are from observed data, since the data is

15

selected for the low-flow season. This gives a more accurate representation of the hydraulic geometry. In Figure 5 (a) and (b), which correspond to the most upstream part, we can observe the presence of floodplains with braided structure of few kilometers, while the rest of the stretch has a confined structure.

5.1.2 ATL13 WSE processing

Initially, we use observations from 236 ATL13 data products, providing measurements in low-flow and high-flow seasons. The 236 ATL13 products contain 3199 WSE points, illustrated by red crosses in Figure 6. The ATL13 quality flags described in section 4.1.3 are applied to the data, removing the largest outliers; the data after applying the quality flags is represented by light blue dots in Figure 6. After applying the extra filtering methods as explained in section 4.1.3, we get 81 WSE observations. These observations cover the calibration period, between November 2018 and September 2020, and are illustrated in Figure 6 by the blue circles. The processing steps provide a good sample of WSE observations, with good spatial coverage of the entire river reach. Moreover, the temporal coverage of the dataset includes low-flow and high-flow season observations, with a slight predominance in the low-flow season, which is related to the quality of ICESat-2 data for the different seasons. The filtering criteria are not biased against high-flow season observations.
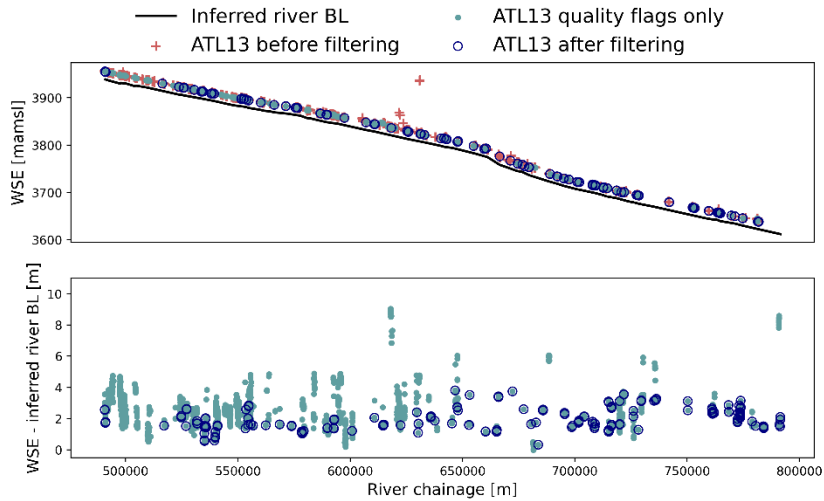

Figure 6. Top: ATL13 WSE along river chainage, before processing, after quality filters are applied and after filtering criteria. Bottom: ATL13 WSE minus inferred BL from the model calibration comparing the quality filters results and the filtering criteria.

### 5.2 Calibration using ICESat-2 observations

To test the sensitivity of the model to the lateral inflow representation, we run two different calibrations. The first one assuming uniform runoff distribution and distribution of boundary inflow according to MERIT flow accumulation map and the second one assuming uniform boundary inflow. Both calibrations are performed against ATL13 WSE observations for four spatially uniform parameters: low-flow depth, Manning's roughness, correction factor α, and cross-section form exponent r. A forward run of the model takes 39 seconds and the hydraulic model calibration converges after about 1000

16

runs. To speed up the calibration, we define discharge classes, in which we group the WSE by the corresponding discharge value in the acquisition date. Acquisition dates with the same discharge value belong to the same class. This way, each iteration includes individual runs for 29 different discharge classes. The minimum RMSE value of the calibration is taken as the optimal value, and results can be seen in Table 1. The RMSE is slightly better using MERIT flow accumulation map than using uniform boundary inflow (0.41 m and 0.42 m respectively), which overall is in good agreement with previous studies (Jiang et al. (2019), Kittel et al. (2020)) considering the low parametrization of the model, which considers uniform depth and roughness. The most sensitive parameters in the FAST sensitivity analysis are Manning's roughness and low-flow depth. Both calibrations improve the RMSE relative to the prior guess, which corresponds to 0.619 m. If we check the parameter space using MERIT flow accumulation calibration the optimal parameter estimate (red diamond in Figure 7) are not close to the a priori interval boundaries, which indicates the parameter constraint was well defined. The most correlated parameters are roughness and depth as seen in Figure 7.

To study the uncertainty of the model we use a Bayesian uncertainty analysis, Differential Adaptive Metropolis (DREAM) algorithm proposed by Vrugt (2016). We run the uncertainty analysis using the MERIT flow accumulation case, which is our best inference result. This algorithm creates a posterior sampling in the parameter space, from which we take the 10 % best model runs to create the posterior distribution.

	Prior	Uniform inflow	MERIT flow acc.	Sensitivity	Uncertainty
RMSE [mamsl]	0.619	0.424	0.414	-	-
Manning's n $[s/m^{1/3}]$	0.031	0.0251	0.02927	0.58	±13%
Depth Y_m^* [m]	2	1.417	1.388	0.884	±11.7%
r	1.8	2.14	1.786	0.072	±28.6%
α $[m/m^3 s^{-1}]$	0.002	0.002121	0.0019045	0.092	±18.4%

Table 1. Steady state solver calibration results for uniform calibration values along the river stretch. The root mean square error (RMSE) is minimized. Uncertainty and sensitivity values correspond to MERIT flow acc. Model. The sensitivity analysis is performed with FAST, and the values represent the ratio between % RMSE change and % of parameter change. The uncertainty of the parameters is computed with DREAM.
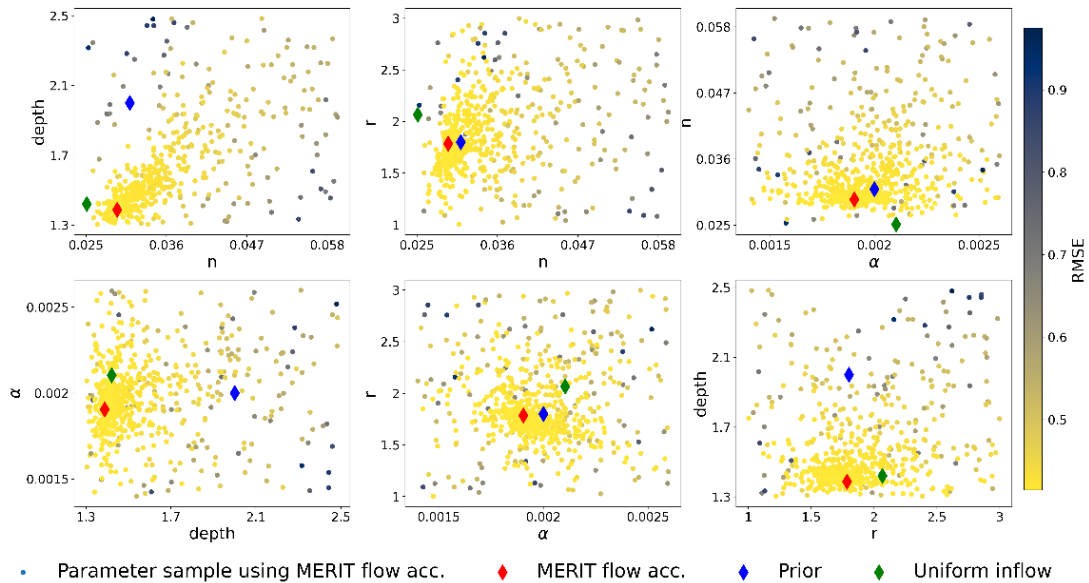
Figure 7. Sampling pattern and model performance during calibration using MERIT flow accumulation map. The objective function is lowered during calibration.

Figure 8 compares the simulated WSE minus inferred bottom level (BL) using MERIT flow accumulation and the ATL13 WSE minus inferred BL. Overall, the simulated WSE corresponds to the ATL13 WSE with a deviation below 1 meter (Figure 8 (a)). The larger errors are found for selected observations in the downstream area and for observations between chainage 650000 m and 680000 m (Figure 8 (b)).
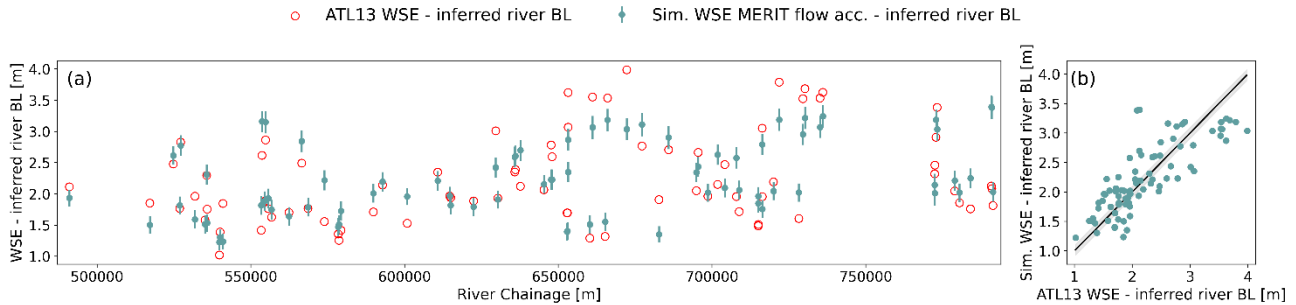
Figure 8. (a) Calibrated longitudinal profile using the steady state solver for uniform depth and MERIT flow accumulation between Jimai and Mentang.(b) Simulated vs. ATL13 WSE minus inferred BL, the shaded area correspond to the mean standard deviation in the ATL13 product, extracted from the flag *stdev_water_surf*.

5.2.1 Validation of the model calibration

The validation data consists of ATL13 observations for the period between 13/12/2020 and 19/10/2021 in which in-situ discharge is used to force the hydraulic model in this period assuming uniform runoff and boundary inflow distributed

18

according to the MERIT flow accumulation map. In the validation period, the RMSE of the model is 44.3 cm, which is in good agreement with the calibration RMSE. The error of the validation data can be seen in Figure 9. The deviation from the
440 ATL13 WSE minus inferred BL goes up to 1.5 m (Figure 9 (a)). We observe again that a larger error is present between chainage 650000 and 680000 m (Figure 9 (b)) as previously seen in the calibration data.
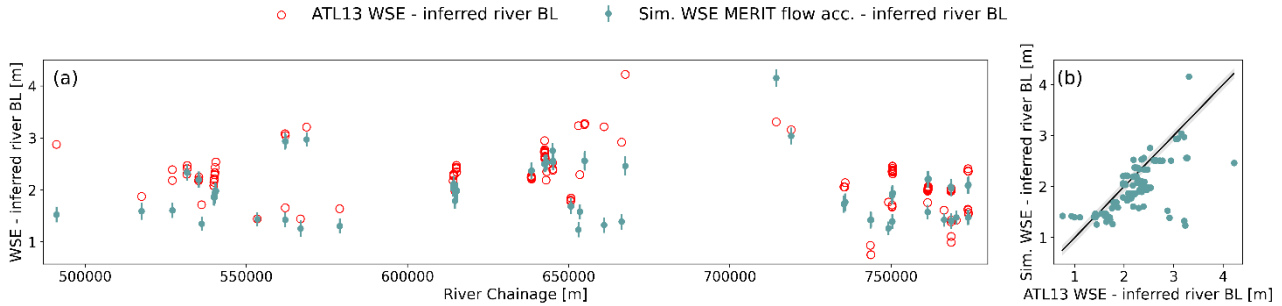

Figure 9. (a) Validation longitudinal profile using the steady state solver for uniform depth and MERIT flow accumulation between Jimai and Mentang.(b) Simulated vs. ATL13 WSE minus inferred BL, the shaded area correspond to the mean standard deviation in the ATL13
445 product, extracted from the flag stdev_water_surf.

5.2.2 Rating curves along the river stretch

The rating curves define the relation between WSE and discharge along the river reach. Rating curves depend on hydraulic characteristics of the
450 channel, so an accurate parametrization is necessary. The relation WSE-discharge generally follows a power law. We calculate rating curves every 50 m from the calibrated hydraulic model. This defines a look up table relating discharge, WSE and river chainage. Examples of rating curves in the look up table are illustrated in Figure 10, where the flow
455 depth, computed as simulated WSE minus calibrated BL, is compared to the discharge. The computed rating curves follow a power law, we can also see that for the more upstream point, 491020 m, the discharge values are lower than the ones more downstream.

Figure 10. Examples of simulated rating curves relating water surface elevation and discharge at different chainage points.

Note that for the relation at chainage 565990 m, the increase in flow depth is larger than other examples. This effect is
460 produced due to the narrower river width at this river location, that produces and increase in flow depth for the same discharge values. This is a clear example of the river geometry effect in building WSE-discharge relationships.
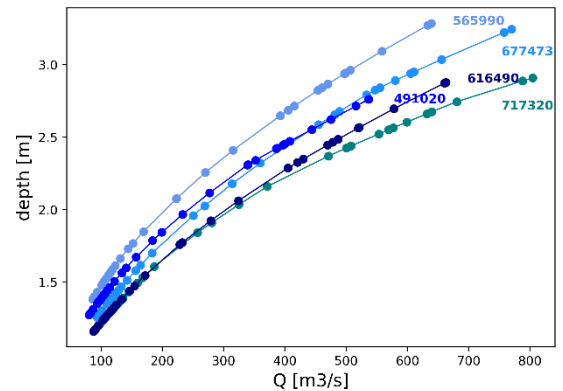
19

5.2.3 Validation of rating relationships and demonstration of model applications

The results of the validation are presented as the percentage of flow exceedance for a given discharge value and are compared with in-situ data (Figure 11, (a) and (b)). The estimated discharge values are for selected ATL13 WSE observations. The validation dataset, corresponding to the period from 13/12/2020 to 19/10/2021, is ingested together with the calibration data in the hydraulic model to interpolate the corresponding discharge at the time of acquisition at a given river location (Jimai and Mentang gauging stations). The estimation using MERIT flow accumulation, uniform boundary inflow and the prior guess are presented. The percentage of flow exceedance for the estimated discharge is in good agreement with the in-situ data for the MERIT flow accumulation case. For Mentang station (Figure 11, (b)), the observed Q60 is about 400 m^3/s , while the simulated Q60 is around 250 m^3/s, which is a considerable difference. For the case using uniform inflow and the prior guess, the difference with in-situ data is larger, mostly for the larger values of discharge, from 400 m^3/s at Jimai and from 500 m^3/s at Mentang. In the simulated discharge we are also calculating low-flow values that are missing in the in-situ measurements, which explains this mismatch.

Table 2 present the RMSE using the 3 different approaches. The best results with the lower RMSE is using MERIT flow accumulation with RMSE 107 m3/s at Jimai and 122.38 m3/s at Mentang. When using the uniform inflow, the difference in RMSE is not significant in Mentang (127.43 m3/s) but it increases at Jimai discharge estimations (149.30 m3/s). In the case of the prior guess, it is quite clear that the results are worse than for the calibrated models.

| In-situ station	Sim. Q MERIT flow acc.	Sim. Q uniform inflow	Sim. Q prior guess
Jimai RMSE [m^3/s]	107.68	149.30	169.98
Mentang RMSE [m^3/s]	122.38	127.43	265.30

Table 2. RMSE between in-situ discharges measured at Jimai and Mentang stations and the estimated discharge. Three different cases are presented, using MERIT flow accumulation map, using uniform inflow and the estimations with the prior guess.
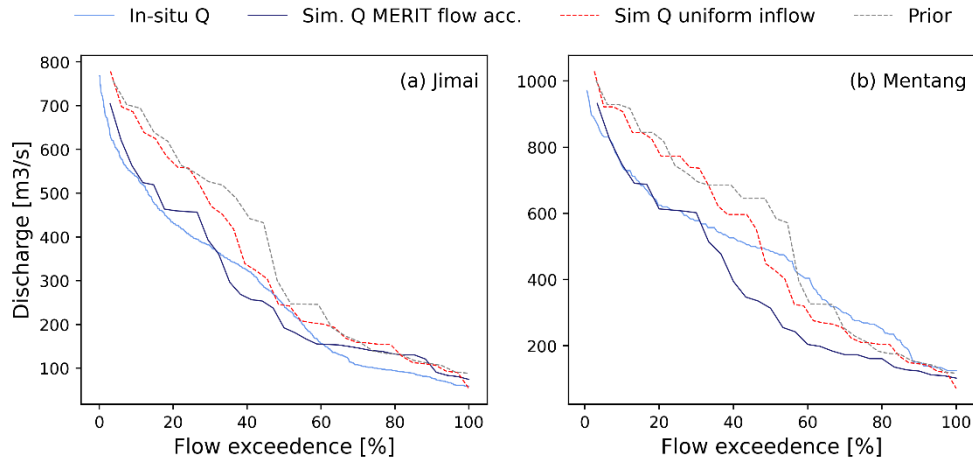
Figure 11. Simulated discharge vs in-situ measured discharge at Jimai (a) and Mentang (b) stations.

There are two different virtual stations (VS) available from Hydroweb in this area of the Yellow River (Normandin, et al. 2018), at kilometre 4914, corresponding to chainage 545030 m, and at kilometre 4901 corresponding to chainage 560360 m. We compare the Sentinel-3 derived Hydroweb VS time series at these two points, with the WSE estimated by the model using MERIT flow accumulation map (Figure 12). The only available ATL13 observation in this area is represented by the blue star in Figure 12 (a), which falls very close to the ATL13 derived WSE time series. It is clear in Figure 12 (a), that the Sentinel-3 deriver WSE are not well represented, probably due to the low resolution of this mission and the mountainous terrain, which reduce the accuracy of the retrieved WSE in this area. The seasonality is not present in the Hydroweb VS time series and some low-flow season values are above the high-flow season values which should not be the case. The offset with the observed and estimated WSE from ATL13, which is expected to perform better due to its resolution, is more than two meters, mostly in the low-flow season. A general bias in the data of this VS can be also observed. In Figure 12 (b), ATL13 derived values match slightly better with the WSE from the VS, however the VS time series present large uncertainties, and the seasonality is poorly represented.

Figure 13 shows examples of WSE ((a), (c) and (e)) and discharge ((b, (d) and (e)) time series for 3 different river locations: at chainage 491020 m, 565990 m and 717320 m. The results are interpolated from ATL13 observations using the WSE-discharge relation at the selected river locations. In-situ measurements for WSE to compare with the simulated values are not available. The figure shows the estimation using MERIT flow accumulation and compares it with the estimation using the uniform inflow and the prior guess. The discharge estimated from the prior and uniform inflow are clearly overestimated compared with the MERIT flow accumulation case, this was also observed in Figure 11, when we compared with in-situ discharge. The main difference from the prior and calibrated parameters, can be seen in Figure 13 (e), at the more upstream example. The larger depth in the prior guess (2 m) is clearly making an impact in this area since we expect to have shallower depth upstream.

21
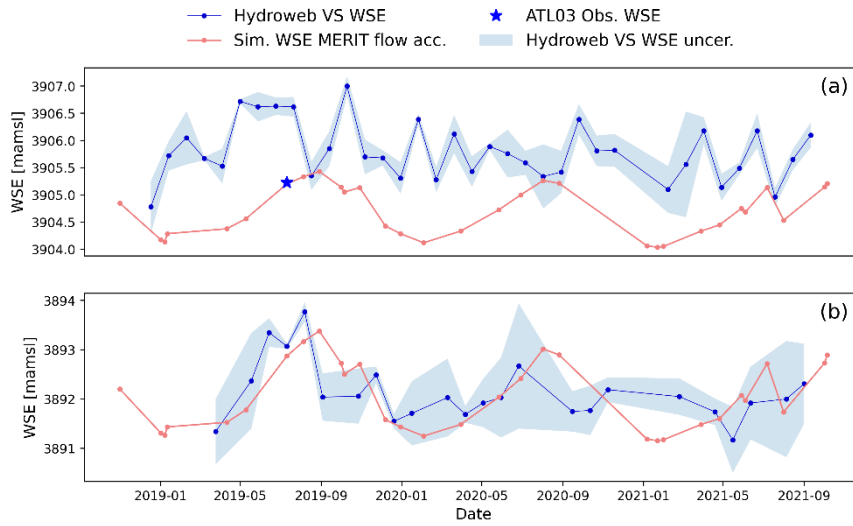
Figure 12. Comparison of estimated WSE with available Hydroweb VS it the AOI. The WSE at VS is derived from Sentinel-3A observations. (a) Simulated WSE at chainage 545030 m vs. WSE at VS 4914 km and (b) Simulated WSE at chainage 560360 m vs. WSE at VS 4901 km.
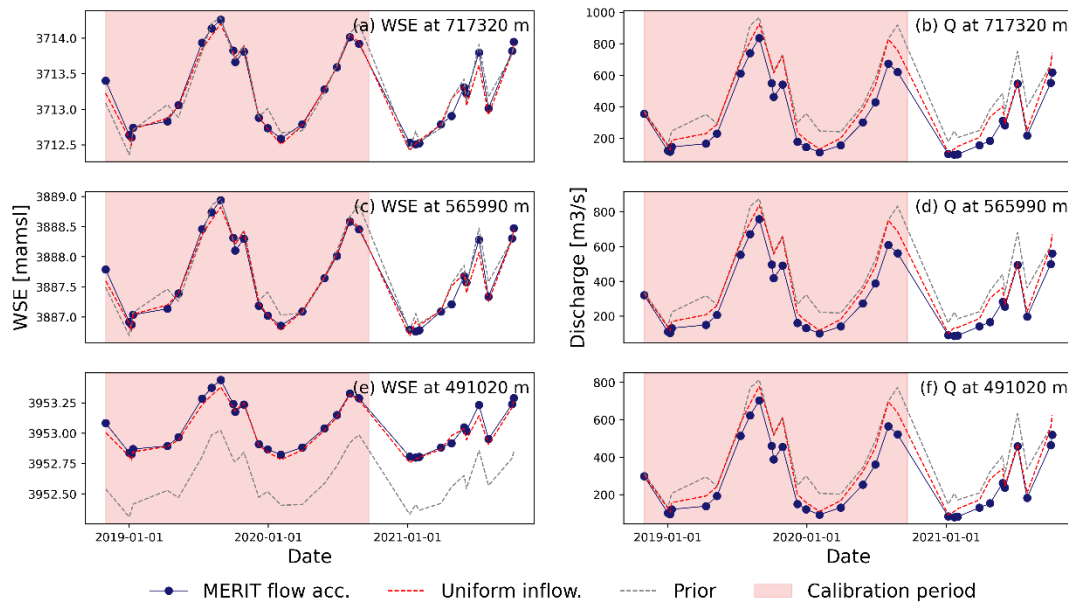

Figure 13. Simulated WSE (a), (c) and (e) and simulated discharge (b), (d) and (f) at selected chainage points. The simulated WSE and Q from MERIT flow acc. inferred parameters is compared with the results using uniform inflow and the prior guess.

5.2.4 Parametrization of HD model

515   The calibrated Manning's roughness, together with the calibrated cross-sections are used in MIKE Hydro River to run a full hydrodynamic model simulation. The model runs in a grid with 1006558 grid points which consist of pairs timestamp-chainage. We define 2 minutes time-steps and 100 m distance. We define a boundary condition at the upstream cross-section with input discharge from Jimai in-situ data, and a

520   downstream boundary at the synthetic cross-section relating discharge and stage. We use the dynamic wave solver that corresponds to the full 1D Saint-Venant equations. Figure 14 (a) compares the simulated WSE by MIKE Hydro and ATL13 WSE minus inferred BL. MIKE simulations seems to be underestimated in most of the cases, and the maximum deviation from the ATL13 WSE minus inferred BL is around 1.7 m.

525   The RMSE is 0.59, which is in good agreement with the results from the steady state solver.

Figure 14 (b) presents the WSE time series at chainage 491020 m simulated from MIKE and from the steady state solver. The time series represent the seasonal variation fairly good. The simulated values from the steady state solver appears to be

530   above the ones from MIKE simulation. This was also observed when we compare the simulated MIKE WSE with the observed ATL13 WSE minus the inferred BL (Figure 14 (a)), which makes sense if we take into account that the simulated water surface from the steady state solver is directly derived from ATL13 observations, while the simulated MIKE WSE is derived from discharge observations.

Figure 14. (a) MIKE Hydro simulated WSE vs. ATL13 WSE minus inferred BL. The shaded area corresponds to the median std. deviation of the ATL13 observations, taken from the flag stdev_water_surf. (b) Simulated WSE from the steady state solver and MIKE.

6 Discussion

6.1 ICESat-2 data selection

ICESat-2 data provides valuable information for river hydraulic modelling. The ATL03 product gives accurate river geometry measurements. The low-flow river width could be retrieved from this product together with measurements of the river dry portion. This is an advantage with respect to other studies in which satellite altimetry could only be used in wider

540   river channels (Leittenmaier, et al. (2015), Kittel, et al. (2020), Jiang, et al. (2019)). The processing of the ATL03 photon cloud dataset provides a well-defined shape of the river cross-section for the non-submerged portion, removing background noise and outliers. Previous studies on hydraulic calibration used hydraulic signatures from satellite remote sensing measurements, but they did not include observations of cross-section geometry, instead they use simplified geometries (Bjerklie, et al. 2018, Pujol, et al. 2020, Garambois, et al. 2020).
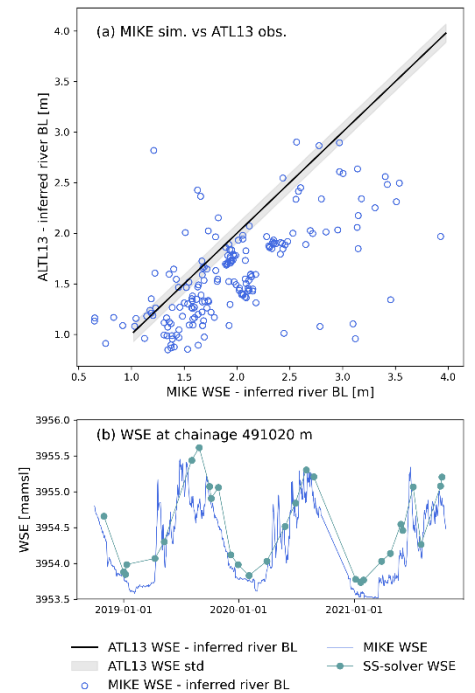
545 The method works best in west-east oriented rivers, where the density of ICESat-2 tracks that are almost perpendicular to the river centreline is highest. However, thanks to the densely spaced ICESat-2 tracks, with an inner track spacing less than 2 km (Markus, et al. 2017), this method can also be used in rivers with dominant south-north orientation, because natural rivers will always include curved reaches where the orientation of the river changes, or where the cross-sections can be corrected and re-projected.

550 Accurate WSE observations are very important in the calibration process. The ATL13 product gives a well distributed sample both in space and time of WSE data. However, several outliers are present, which need a closer look. Besides the quality flags that the product provides, an outlier filtering process was defined based on the water occurrence and river centre-line. Applying these two criteria, the main outliers were successfully removed without rejecting good quality observations.

555 The main drawback of ICESat-2 data, is the inability to operate in all weather conditions, since laser altimeter cannot penetrate thick clouds. This creates gaps in the cross-section data of up to 10 km. However, future acquisitions on the corresponding ground tracks can be used to fill these gaps.

6.2 Model performance

We presented a spatially uniform flow depth and roughness calibration against ATL13 WSE. The steady state assumption
560 and low parametrization with only four calibration parameters, makes the model converge fast using a global search algorithm. Two different calibrations were compared to check the model sensitivity to lateral inflows, one using MERIT flow accumulation map, and one assuming uniform inflow. The best calibration resulted from the MERIT flow accumulation case with RSME value of 0.41 m. This result was quite satisfactory with respect to other studies which used distributed depth calibration and applied it to wider river channels. Indeed, Jiang, et al. (2019) obtained a RMSE between 0.72 and 1.6 m
565 using combination of altimetry datasets over the Songhua River. Kittel, et al. (2021) presents RMSE between 0.61 and 0.89 m using Cryosat-2 observations only on the Zambezi Catchment. Pujol, et al. (2020) uses ENVISAT observations and Synthetic SWOT to infer channel geometries, resulting in WSE RMSEs around 0.94 m. When using a multi-mission approach, Domeneghetti et al. (2021) reports RMSEs between 0.68 m and 0.89 m in the Po River, The parameters most sensitive to the calibration were the roughness coefficient and the low-flow depth, while the cross-section form exponent and
570 correction factor had a lower impact. The value of the cross-section form exponent is most uncertain, however changes in this value do not introduce large changes in the model. Additionally to the uniform depth calibration, we attempted to calibrate distributed depth models, which did not improve the RMSE. The test was made for 5 and 10 uniformly distributed depths along the river reach with uniform Manning's roughness. Defining more parameters in the model increases the computational cost significantly and convergence could not be reached in some cases. We observed a larger error between
575 simulated and observed depth between chainage 650000 and 680000 m, that was not removed when calibrating distributed depths. The WSE in this area seems underestimated for high-flow observations and overestimated for low-flow observations.

A validation dataset for a 10-month period is used, in which the RMSE is 0.44 m, in good agreement with the calibration data. The same larger error were observed between chainage 650000 and 680000 m.

In addition, we ran calibrations using 8 and 16 distributed Manning's roughness, where the RMSE improves to 0.377 and 580 0.365 m respectively. However, when evaluating the validation data, the RMSE for 8 and 16 distributed roughness is 0.445 and 0.425 m respectively (see appendix A). The first case is an indicator of over-fitting in the model. Increasing the distributed roughness coefficient to 16 reduces the RMSE by a few centimetres, but the computational cost of the calibration increases significantly.

Overall the model performance is satisfactory compared to previous studies, with the added value of being a low 585 parametrized model. In addition, the steady-state assumption reduces significantly the simulation time, which took 1h and 15 min for a period of 3 years in a full 1D hydrodynamic simulation, compared with the 39 seconds of steady state forward run for all the discharge classes. These two factors make the convergence of the calibration process quite fast.

6.3 WSE densification and discharge estimation

ICESat-2 altimetry provides accurate elevation measurements at low temporal resolution. To create WSE and discharge time 590 series, interpolation of WSE is needed. We use the calibrated hydraulic model to create WSE-discharge relationships in the form of rating curves along the river stretch, an approach that has been previously used in other studies successfully (Malou, et al. 2021). Rating curves make possible the interpolation of WSE and estimation of discharge at any point in the river for a given ATL13 WSE observation.

In Figure 11 we compare the estimated discharge with the available in-situ discharge at Jimai and Mentang stations in % of 595 flow exceedance. The estimations are reasonably good when we use the MERIT flow accumulation. Simplifying the model to uniform boundary inflow accentuates the error at the upstream end, which shows the importance of defining the prior inflows accurately (Garambois, et al. 2020). Examples of interpolated WSE and discharge at different chainage points are also provided in Figure 13. These results could not be compared with in-situ observations, since these areas are ungauged. With the method we present, the interpolation can be made for the available ICESat-2 acquisitions, which also need 600 processing and outlier removal. It is important to note, that for every river point, ICESat-2 crosses at the same exact point every 91 days, while for the interpolated time series we have up to 3 valid values per month. Observations from other altimetry missions such as Cryosat-2 or Sentinel-3 are challenging to incorporate in the model, since the flow width is smaller than the along-track resolution of these missions; the available Hydroweb VS time series derived from Sentinel-3A do not show great results (see Figure 12). The SWOT upcoming satellite mission will be able to measure rivers down to 50 605 meters wide, representing a promising opportunity to incorporate new WSE observables into the model using a multi-mission approach as in other studies (Domeneghetti, Molari, et al. 2021).

25

6.4 Parametrization of HD models

The calibrated parameters were included in MIKE Hydro River to run a full hydrodynamic model using the dynamic wave solver. The model is numerically stable defining 2 minutes time steps and 100 m chainage steps, creating a grid with 1006558 points. The model simulation takes 1 hour 15 minutes to finish. If we compare this run time with the 39 seconds of a forward run in the steady state solver, we can clearly see that a full hydrodynamic simulation is not suitable for calibration. The results presents a larger RMSE of 0.59 m with respect to the RMSE using the steady state solver of 0.41 m. Figure 14**Error! Reference source not found.** shows that most of the simulated depth are underestimated. The difference in the simulation performance between the steady state calibration and the full hydrodynamic model can be related to the simplification made by the steady state assumption.

7 Conclusions

In this study we present a method for river hydraulic parameter calibration that can be used to estimate discharge and interpolate WSE from altimetry observations. The main novelty of the method is the incorporation of exposed cross-sectional geometry from ICESat-2 ATL03 product, which greatly facilitates river modelling in narrow rivers with flow width below 100 m. Previous radar altimetry missions such as Cryosat-2, Sentinel-2 or Jason-2 did not provide such measurements due to its lower resolution with microwaves.

The hydraulic model calibration is performed against ATL13 WSE observations. The model has a low parametrization, which together with the steady state assumption makes the calibration converge fast. The resulting RMSE is of 0.41 m, and of 0.44 m when using the validation dataset. These values are in good agreement with previous studies that used larger parametrization. The calibrated model provides estimations of WSE and discharge along the entire river stretch for a given ATL13 WSE observation. The estimated discharge at Jimai and Mentang is in good agreement with the in-situ discharge measure at the gauging stations, with and RMSE of 107 m^3/s 7 at Jimai and 122 m^3/s at Mentang.

This study for the first time demonstrated the value of ICESat-2 in river hydraulic modelling, which is especially useful for poorly gauged or remote river basins. The ICESat-2 mission performs better than previous altimetry missions that were limited to wide river channels. Using a simplified hydraulic model, with steady state assumption and low parametrization we achieve good results at a reduced computational cost than full 1D hydrodynamic models.

Appendix A: Distributed Manning's roughness calibration

The appendix includes the result of the distributed Manning's roughness calibration and compares it with the uniform calibration results.
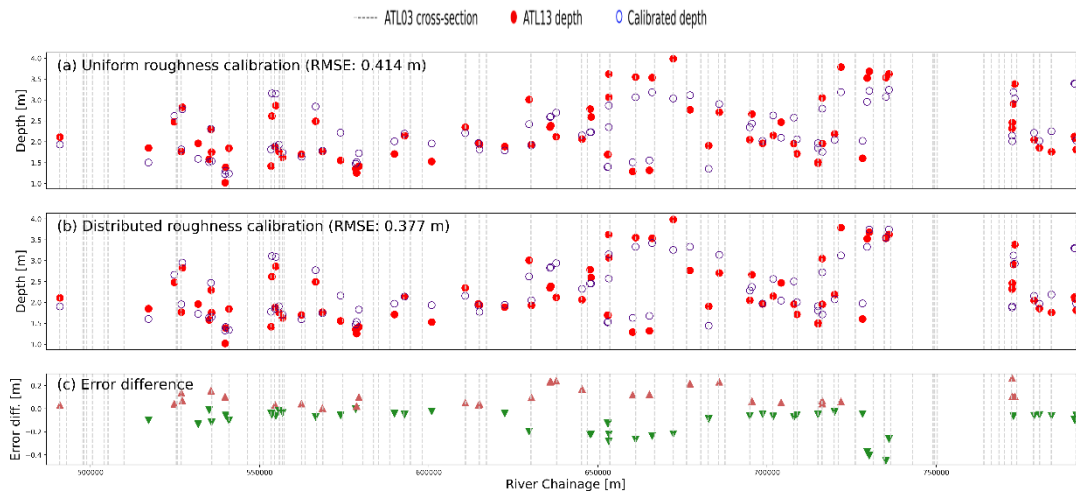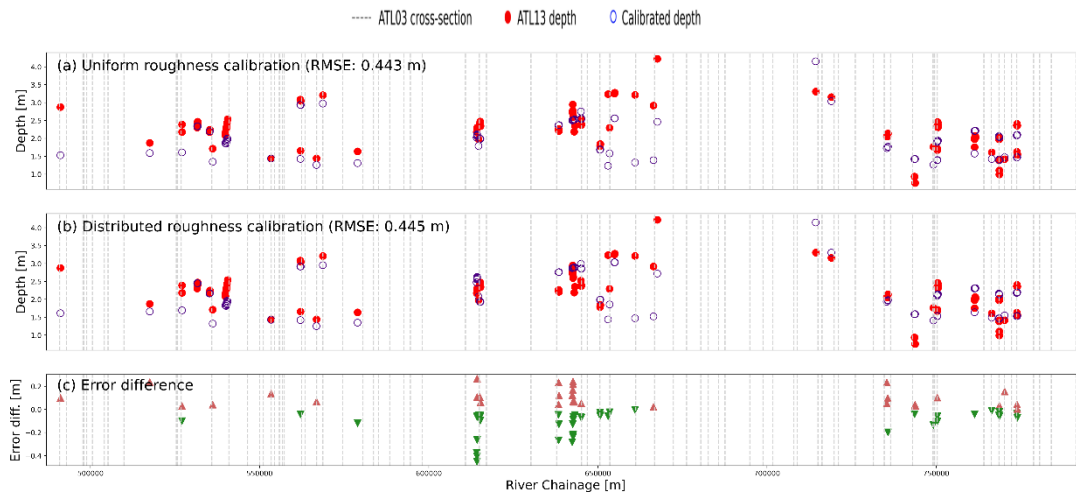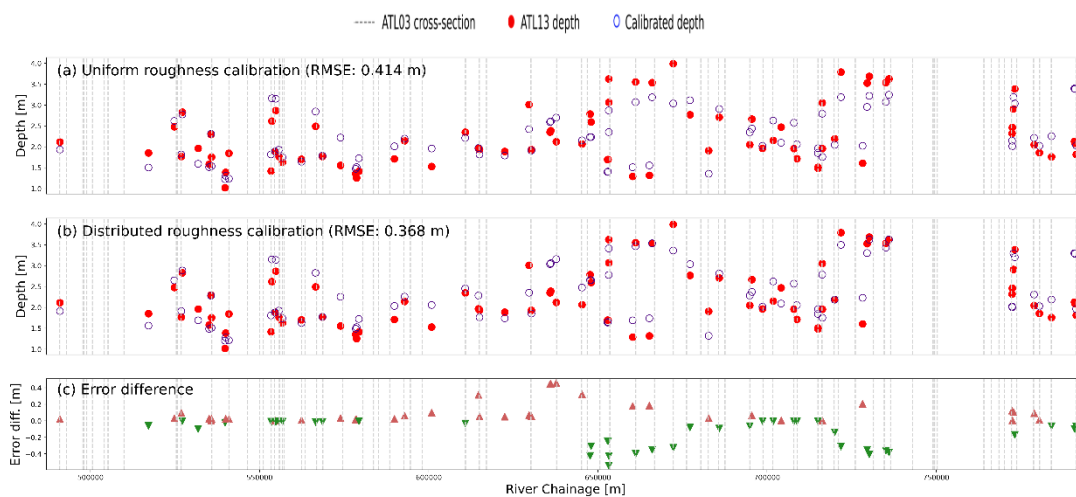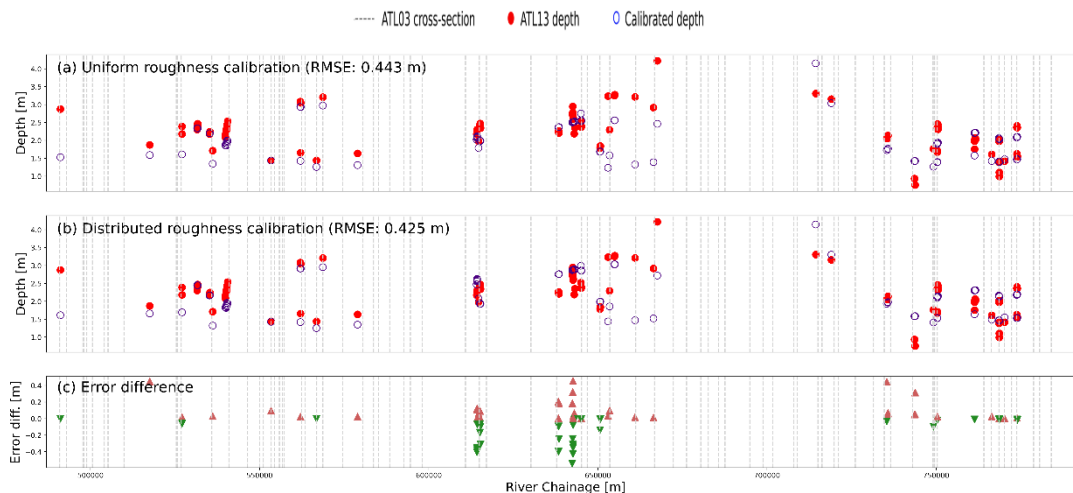
Figure A1. Uniform depth calibration (a) compared with distributed roughness calibration (b) for 8 Manning's roughness and error difference between the uniform calibration and the distributed calibration (c).

650 **Figure A2.** Validation data error for uniform depth calibration (a), distributed roughness calibration for 8 Manning's roughness (b) and error difference between the uniform calibration and the distributed calibration (c).

Figure A3. Uniform depth calibration (a) compared with distributed roughness calibration (b) for 16 Manning's roughness and error difference between the uniform calibration and the distributed calibration (c).

28

Figure A4. Validation data error for uniform depth calibration (a), distributed roughness calibration for 16 Manning's roughness (b) and error difference between the uniform calibration and the distributed calibration (c).

655

660

665

670

675

Bibliography

Bjerklie, David M., Charon M. Birkett, John W. Jones, Claudia Carabajal, Jennifer A. Rover, John W. Fulton, and Pierre-André Garambois. 2018. "Satellite remote sensing estimation of river discharge: Application to the Yukon River Alaska." *Journal of Hydrology* 561: 1000-1018. doi:https://doi.org/10.1016/j.jhydrol.2018.04.005.

Boergens, E., S. Buhl, D. Dettmering, C. Kluppelberg, and F. Seitz. 2016. "Combination of multi-mission altimetry data along the Mekong River with spatio-temporal kriging." *Journal of Geodesy* 1-16. doi:10.1007/s00190-016-0980-z.

Chen, Yuxin, Anja Vogel, Cameron Wagg, Tianyang Xu, Maitane Iturrate-Garcia, Michael Scherer-Lorenzen, Alexandra Weigelt, Nico Eisenhauer, and Bernhard Schmid. 2022. "Drought-exposure history increases complementarity between plant species in response to a subsequent drought." *NATURE COMMUNICATIONS* 13. doi:10.1038/s41467-022-30954-9.

Dingman, S. 2007. "Analytical Derivation of At-a-Station Hydraulic-Geometry Relations." *Journal of Hydrology - J HYDROL* 334: 17-27. doi:10.1016/j.jhydrol.2006.09.021.

Domeneghetti, Alessio, Angelica Tarpanelli, Luca Brocca, Silvia Barbetta, Tommaso Moramarco, Attilio Castellarin, and Armando Brath. 2014. "The use of remote sensing-derived water surface data for hydraulic model calibration." *Remote Sensing of Environment* 149: 130-141. doi:https://doi.org/10.1016/j.rse.2014.04.007.

Domeneghetti, Alessio, Giada Molari, Mohammad J. Tourian, Angelica Tarpanelli, Sajedeh Behnia, Tommaso Moramarco, Nico Sneeuw, and Armando Brath. 2021. "Testing the use of single- and multi-mission satellite altimetry for the calibration of hydraulic models." *Advances in Water Resources* 151: 103887. doi:https://doi.org/10.1016/j.advwatres.2021.103887.

Duan, Qingyun, Soroosh Sorooshian, and Vijai Gupta. 1992. "Effective and efficient global optimization for conceptual rainfall-runoff models." *Water Resources Research* 28: 1015-1031. doi:https://doi.org/10.1029/91WR02985.

Duan, Vijai, and Soroosh Sorooshian. 1993. "Shuffled complex evolution approach for effective and efficient global minimization." *Journal of Optimization Theory and Applications* 76: 1573-2878. doi:https://doi.org/10.1007/BF00939380.

Durand, Michael, Jeffrey Neal, Ernesto Rodríguez, Konstantinos M. Andreadis, Laurence C. Smith, and Yeosang Yoon. 2014. "Estimating reach-averaged discharge for the River Severn from measurements of river water surface elevation and slope." *Journal of Hydrology* 511: 92-104. doi:https://doi.org/10.1016/j.jhydrol.2013.12.050.

Garambois, P.-A., K. Larnier, J. Monnier, P. Finaud-Guyot, J. Verley, A.-S. Montazem, and S. Calmant. 2020. "Variational estimation of effective channel and ungauged anabranching river discharge from multi-satellite water heights of different spatial sparsity." *Journal of Hydrology* 581: 124409. doi:https://doi.org/10.1016/j.jhydrol.2019.124409.

Garambois, Pierre-André, and Jérôme Monnier. 2015. "Inference of effective river properties from remotely sensed observations of water surface." *Advances in Water Resources* 79: 103-120. doi:https://doi.org/10.1016/j.advwatres.2015.02.007.

680

685

690

695

700

705

Havnø, K., M. N. Madsen, and J. Dørge. 1995. "MIKE 11 - a generalized river modelling package." *Computer models of watershed hydrology* (Water Resources Publications) 733-782.

Houska, Tobias, Philipp Kraft, Alejandro Chamorro-Chavez, and Lutz Breuer. 2015. "SPOTting Model Parameters Using a Ready-Made Python Package." *PLOS ONE* (Public Library of Science) 10: 1-22. doi:10.1371/journal.pone.0145180.

Jasinski, M., J. Stoll, D. Hancock, J. Robbins, J. Nattala, T. Pavelsky, J. Morrison, et al. 2021. "Algorithm Theoretical Basis Document (ATBD) for Along Track Inland Surface Water Data, ATL13, Release 5." doi:10.5067/RI5QTGTSVHRZ.

Jasinski, M., J. Stoll, D. Hancock, J. Robbins, J. Nattala, T. Pavelsky, J. Morrison, et al. 2021. "ATL13 Along Track Surface Water Data, Release 004 Algorithm Notes and Known Issues." doi:10.5067/RNI05Y2CJ9FV.

Jasinski, M., J. Stoll, D. Hancock, J. Robbins, J. Nattala, T. Pavelsky, J. Morrison, et al. 2021. "ATLAS/ICESat-2 L3A Along Track Inland Surface Water Data, Release 5." doi:10.5067/ATLAS/ATL13.005.

Jiang, Liguang, Henrik Madsen, and Peter Bauer-Gottwein. 2019. "Simultaneous calibration of multiple hydrodynamic model parameters using satellite altimetry observations of water surface elevation in the Songhua River." *Remote Sensing of Environment* 229-247. doi:10.1016/j.rse.2019.03.014.

Jiang, Liguang, Raphael Schneider, Ole B. Andersen, and Peter Bauer-Gottwein. 2017. "CryoSat-2 Altimetry Applications over Rivers and Lakes." *Water* 9. doi:10.3390/w9030211.

Kittel, C. M. M., L. Jiang, C. Tøttrup, and P. Bauer-Gottwein. 2020. "Sentinel-3 radar altimetry for river monitoring – a catchment-scale evaluation of satellite water surface elevation from Sentinel-3A and Sentinel-3B." *Hydrology and Earth System Sciences* 25: 333–357. doi:10.5194/hess-25-333-2021.

Kittel, C. M. M., L. Jiang, C. Tøttrup, and P. Bauer-Gottwein. 2020. "Sentinel-3 radar altimetry for river monitoring: a catchment-scale evaluation of satellite water surface elevation from Sentinel-3A and Sentinel-3B." *Hydrology and Earth System Sciences* 333-357. doi:10.5194/hess-25-333-2021.

Kittel, Cecile M. M., Simbidzayi Hatchard, Jeffrey C. Neal, Karina Nielsen, Paul D. Bates, and Peter Bauer-Gottwein. 2021. "Hydraulic Model Calibration Using CryoSat-2 Observations in the Zambezi Catchment." *Water Resources Research* 57: e2020WR029261. doi:https://doi.org/10.1029/2020WR029261.

Larsen, Stefano, Ute Karaus, Cecile Claret, Ferdinand Sporka, Ladislav Hamerlík, and Klement Tockner. 2019. "Flooding and hydrologic connectivity modulate community assembly in a dynamic river-floodplain ecosystem." *PLOS ONE* (Public Library of Science) 14: 1-22. doi:10.1371/journal.pone.0213227.

Lettenmaier, Dennis P., Doug Alsdorf, Jeff Dozier, George J. Huffman, Ming Pan, and Eric F. Wood. 2015. "Inroads of remote sensing into hydrologic science during the WRR era." *Water Resources Research* 51: 7309-7342. doi:https://doi.org/10.1002/2015WR017616.

Li, Yibao, Jung-I. I. Choi, Yongho Choic, and Junseok Kim. 2017. "A simple and efficient outflow boundary condition for the incompressible Navier–Stokes equations." *Engineering Applications of Computational Fluid Mechanics* (Taylor & Francis) 11: 69-85. doi:10.1080/19942060.2016.1247296.

Malou, T., P.-A . Garambois, A. Paris, J. Monnier, and K. Larnier. 2021. "Generation and analysis of stage-fall-discharge laws from coupled hydrological-hydraulic river network model integrating sparse multi-satellite data." *Journal of Hydrology* 603: 126993. doi:https://doi.org/10.1016/j.jhydrol.2021.126993.

Markus, Thorsten, Tom Neumann, Anthony Martino, Waleed Abdalati, Kelly Brunt, Beata Csatho, Sinead Farrell, et al. 2017. "The Ice, Cloud, and land Elevation Satellite-2 (ICESat-2): Science requirements, concept, and implementation,." *Remote Sensing of Environment.*

Masson-Delmotte V., Pirani A. Connors S. L. Péan C. Berger S. Caud N. Chen Y. Goldfarb L. Gomis M. I. Huang M. Leitzell K. Lonnoy E. Matthews J. B. R. Maycock T. K. Waterfield T. Yelekçi O. Yu R., and B.. Zhou. 2021. "Climate Change 2021: The Physical Science Basis. Contribution of Working Group I to the Sixth Assessment Report of the Intergovernmental Panel on Climate Change." *Cambridge University Press* 6.

Nelder, J. A., and R. Mead. 1965. "A Simplex Method for Function Minimization." *The Computer Journal* 7: 308-313. doi:10.1093/comjnl/7.4.308.

Neumann T., A., A. Brenner, D. Hancock, J. Robbins, J. Saba, K. Harbeck, A. Gibbons, et al. 2021. "ATLAS/ICESat-2 L2A Global Geolocated Photon Data, Version 5." *NASA National Snow and Ice Data Center Distributed Active Archive Center* 5. doi:https://doi.org/10.5067/ATLAS/ATL03.005.

Nielsen, Karina, Elena Zakharova, Angelica Tarpanelli, Ole B. Andersen, and Jérôme Benveniste. 2022. "River levels from multi mission altimetry, a statistical approach." *Remote Sensing of Environment* 270: 112876. doi:https://doi.org/10.1016/j.rse.2021.112876.

Normandin, Cassandra, Frappart Frédéric, Adama Telly Diepkilé, Vincent Marieu, Eric Mougin, Fabien: Lubac, Bertrand Blarel, Nadine Braquet, and Abdramane Ba. 2018. "Evolution of the Performances of Radar Altimetry Missions from ERS-2 to Sentinel-3A over the Inner Niger Delta." *Remote Sensing* 833. doi:10.3390/rs10060833.

Paiva, R. C. D., W. Collischonn, M.-P. Bonnet, L. G. G. de Gonçalves, S. Calmant, A. Getirana, and J. Santos da Silva. 2013. "Assimilating in situ and radar altimetry data into a large-scale hydrologic-hydrodynamic model for streamflow forecast in the Amazon." *Hydrology and Earth System Sciences* 17: 2929–2946. doi:10.5194/hess-17-2929-2013.

Paiva, Rodrigo C. D., Michael T. Durand, and Faisal Hossain. 2015. "Spatiotemporal interpolation of discharge across a river network by using synthetic SWOT satellite data." *Water Resources Research* 51: 430-449. doi:https://doi.org/10.1002/2014WR015618.

Paris, Adrien, Rodrigo Dias de Paiva, Joecila Santos da Silva, Daniel Medeiros Moreira, Stephane Calmant, Pierre-André Garambois, Walter Collischonn, Marie-Paule Bonnet, and Frederique Seyler. 2016. "Stage-discharge rating curves

based on satellite altimetry and modeled discharge in the Amazon basin." *Water Resources Research* 52: 3787-3814. doi:https://doi.org/10.1002/2014WR016618.

Parrish, Christopher E., Lori A. Magruder, Amy L. Neuenschwander, Nicholas Forfinski-Sarkozi, Michael Alonzo, and Michael Jasinski. 2019. "Validation of ICESat-2 ATLAS Bathymetry and Analysis of ATLAS's Bathymetric Mapping Performance." *Remote Sensing* 11. doi:10.3390/rs11141634.

Pekel, Jean-François, Andrew Cottam, Noel Gorelick, and Alan S. Belward. 2016. "High-resolution mapping of global surface water and its long-term changes." *Nature (London)* (Nature Publishing Group) 540: 418-422.

Pujol, L., P.-A. Garambois, P. Finaud-Guyot, J. Monnier, K. Larnier, R. Mosé, S. Biancamaria, et al. 2020. "Estimation of multiple inflows and effective channel by assimilation of multi-satellite hydraulic signatures: The ungauged anabranching Negro river." *Journal of Hydrology* 591: 125331. doi:https://doi.org/10.1016/j.jhydrol.2020.125331.

Saltelli, A., S. Tarantola, and K. P.-S. Chan. 1999. "A Quantitative Model-Independent Method for Global Sensitivity Analysis of Model Output." *Technometrics* (Taylor & Francis) 41: 39-56. doi:10.1080/00401706.1999.10485594.

Scherer, Daniel, Christian Schwatke, Denise Dettmering, and Florian Seitz. 2022. "ICESat-2 Based River Surface Slope and Its Impact on Water Level Time Series From Satellite Altimetry." *Water Resources Research* e2022WR032842. doi:https://doi.org/10.1029/2022WR032842.

Shen, Youjiang, Dedi Liu, Liguang Jiang, Jiabo Yin, Karina Nielsen, Peter Bauer-Gottwein, Shenglian Guo, and Jun Wang. 2020. "On the Contribution of Satellite Altimetry-Derived Water Surface Elevation to Hydrodynamic Model Calibration in the Han River." *Remote Sensing* 12. doi:10.3390/rs12244087.

Tarpanelli, Angelica, Stefania Camici, Karina Nielsen, Luca Brocca, Tommaso Moramarco, and Jérôme Benveniste. 2021. "Potentials and limitations of Sentinel-3 for river discharge assessment." *Advances in Space Research* 68: 593-606. doi:https://doi.org/10.1016/j.asr.2019.08.005.

Villadsen, H., O. Andersen, L. Stenseng, K. Nielsen, and P. Knudsen. 2015. "CryoSat-2 altimetry for river level monitoring - Evaluation in the Ganges-Brahmaputra River basin." *Remote Sensing of Environment* 168: 80-89. doi:10.1016/j.rse.2015.05.025.

Vrugt, Jasper A. 2016. "Markov chain Monte Carlo simulation using the DREAM software package: Theory, concepts, and MATLAB implementation." *Environmental Modelling & Software* 75: 273-316. doi:https://doi.org/10.1016/j.envsoft.2015.08.013.

Xu, Nan, Huiying Zheng, Yue Ma, Jian Yang, Xinyuan Liu, and Xiaohua Wang. 2021. "Global Estimation and Assessment of Monthly Lake/Reservoir Water Level Changes Using ICESat-2 ATL13 Products." *Remote Sensing* 13. doi:10.3390/rs13142744.

Yamazaki, D., D. Ikeshima, J. Sosa, P. D. Bates, G. H. Allen, and T. M. Pavelsky. 2019. "MERIT Hydro: A high-resolution global hydrography map based on latest topography datasets." *Water Resources Research* 55: pp.5053-5073. doi:10.1029/2019WR024873.

Yoon, Yeosang, Michael Durand, Carolyn Merry, and Ernesto Rodriguez. 2013. "Improving Temporal Coverage of the SWOT Mission Using Spatiotemporal Kriging." *Selected Topics in Applied Earth Observations and Remote Sensing, IEEE Journal of* 6: 1719-1729. doi:10.1109/JSTARS.2013.2257697.

810   Zhang, Yadong, Zongkun Li, Wei Ge, Xudong Chen, Hongyin Xu, and Hongyan Guan. 2021. "Evaluation of the impact of extreme floods on the biodiversity of terrestrial animals." *Science of The Total Environment* 790: 148227. doi:https://doi.org/10.1016/j.scitotenv.2021.148227.